Tailoring Binder-Cathode Interactions for Long-Life Room-Temperature Sodium-Sulfur Batteries

Alex Yong Sheng Eng,[a] Dan-Thien Nguyen,[a] Vipin Kumar,[a] Gomathy Sandhya Subramanian,[a] Man-Fai Ng,[b] Zhi Wei Seh[a]*

[a] Institute of Materials Research and Engineering, Agency for Science, Technology and Research (A*STAR), 2 Fusionopolis Way, Innovis, Singapore 138634, Singapore

[b] Institute of High Performance Computing, Agency for Science, Technology and Research (A*STAR), 1 Fusionopolis Way, Connexis, Singapore 138632, Singapore

Corresponding author email: sehzw@imre.a-star.edu.sg

Abstract

Room-temperature sodium-sulfur batteries (NaSBs) are well poised as candidates for next-generation battery applications. However, two important limitations must first be overcome: irreversible capacity loss from long-chain polysulfide dissolution, and cathode pulverization from severe volume expansion. Although covalent-sulfur composites like sulfurized polyacrylonitrile (S-PAN) prevent polysulfide dissolution, they do not address the latter issue in sustaining the cathode structure during the sodiation reaction. In this work, we demonstrate that the unique interactions between polar binders and insoluble short-chain sulfur species can be exploited as a strategy to solve both challenges concurrently. Our hypothesis is that specific polar groups, like the *carboxyl* moiety, interact strongly with sodium sulfide and short-chain polysulfides, as compared to traditional fluoropolymer binders employed in most sulfur-based cathodes. Binder-cathode interactions were first predicted for sodium-sulfur batteries using theoretical calculations, then confirmed experimentally using polyacrylic acid (PAA) binder, in combination with a S-PAN cathode. This strategy can be further generalized to other carboxyl binder systems, as demonstrated by two additional binders derived from natural products. Compared to conventional polyvinylidene difluoride-based cathodes

Journal of Materials Chemistry A Accepted Manuscript

experiencing large initial capacity losses, the PAA-based S-PAN cathode delivered a long 1000 cycle lifetime with initial and final discharge capacities of 1195 and 1000 mAh·$g_{(S)}^{-1}$ respectively, representing a low capacity loss of 0.016% per cycle. Rational design of NaSBs based on the synergistic interactions between insoluble sulfur species and carboxyl-binders allows us to overcome key challenges for their practical development.

1. Introduction

In the conduct of our daily lives, we encounter numerous devices and applications based on lithium-ion batteries (LIBs) for our energy storage requirements.[1] LIBs typically employ costly metals which include cobalt, nickel, and lithium itself. Our reliance on these raw materials subject us to economic considerations associated with their scarcity and high cost volatility, making LIBs particularly unsuited for large-scale deployments such as grid-level energy storage.[2,3] Today, sodium-based batteries are emerging with the potential to overtake current lithium-ion technologies for such large-scale applications. Compared to lithium, sodium is abundant in the Earth's crust, making it a significantly cheaper anode. When coupled together with sulfur cathode, room-temperature sodium-sulfur batteries (NaSBs) can improve cost-effectiveness, while at the same time delivering high specific capacities. Nonetheless, several key challenges impede their adoption for practical energy storage. Considering the similarities in sulfur-based cathode chemistries, issues that plague lithium-sulfur batteries[4,5,6] continue to affect NaSBs.[2,3,7] In fact, some problems are further exacerbated due to the larger size and weight of Na^+ ion, and the higher reactivity of sodium metal.

One major issue faced by sulfur-based cathodes is repetitive volumetric expansion and contraction cycles. Over time, this significantly degrades the structural integrity of the cathode, causing poor capacity retention and cycling stability. Given the densities of sulfur,

lithium sulfide, sodium sulfide (2.03 g cm^{-3}, 1.66 g cm^{-3}, 1.86 g cm^{-3}) and their respective molecular weights, the S → Li$_2$S conversion undergoes a volume expansion of approximately 80%.[4] In contrast, the same cathode S → Na$_2$S is expected to experience a significantly more severe expansion of 170% when applied in the NaSB system, leading to greater pulverization of the material.

A second challenge of NaSBs is the dissolution of long-chain polysulfides from the cathode and the consequent shuttle effect.[2,7,8] While the high reactivity of the Na anode can be mitigated by forming alloying interphases[9-11] or other stable solid electrolyte interphases (SEIs),[12-15] these methods do not prevent capacity loss due to polysulfide dissolution into the electrolyte. To this end, several strategies have been taken to confine *soluble long-chain* polysulfides within the cathode architecture. These methods may include separator modification,[16,17] interlayers,[18] solid and polymer electrolytes,[19-25] to recent approaches of physically encapsulating the active species,[26] or the use of novel hosts to regulate or catalyze these soluble polysulfides.[12,27-32] Alternatively, a strategy to eliminate the presence of soluble polysulfides can also be adopted, by employing only *insoluble short-chain* sulfur species. Such short-chain sulfur molecules (typically S$_{2-4}$) could be created either by confinement within the pores of microporous carbons,[10,15,33-35] or formed through covalent bonding to a composite structure,[36-38] where different carbon-sulfur chain lengths can be specifically controlled.[39,40] Consequently, a major advantage of these insoluble sulfur species is their compatibility with standard carbonate electrolytes, unlike soluble long-chain polysulfides that irreversibly react with alkyl carbonates.

Such composites are typically termed sulfurized carbons, and several variations of sulfurized polyacrylonitrile (S-PAN) composites have been demonstrated with NaSBs. The first attempt by Wang *et al.* in 2007 attained a short battery lifetime of just 18 cycles, and required atypical cathode assembly using porous nickel foam.[38] Subsequent reports employed

electrospinning of fibers to improve both cycle life and rate performance,[36,37] as a means to circumvent the reputedly low electronic conductivity and slow Na$^+$ ion diffusion in the dense composite.[41] As a result, conventional battery manufacturing methods like slurry-based cathode preparation and roll-to-roll processing cannot be employed for large scale production. More recently, efforts have instead been focused on accelerating the reaction kinetics of the S-PAN redox conversion by chemical doping with selenium, tellurium, or iodine.[41-44] Nevertheless, such doping with heavier elements introduces yet another issue as the added weight reduces the overall energy density of the cell. An undoped composite with particulate morphology would therefore be advantageous.

Based on insight from lithium batteries, it is recognized that certain binders interact more favorably with some materials as compared to others, and is one fundamental approach to address issues associated with electrode volume expansion.[45-52] In lithium-sulfur cathodes for example, density functional theory calculations have shown that certain polar groups such as amines and amides act as polysulfide anchors to prevent their dissolution, and also impart good mechanical properties.[45,53] Despite the greater severity of pulverization predicted for the sodium-sulfur system, there have been no comparative studies as yet on functional binder effects in NaSB cathodes, to the best of our knowledge.

In this report, we first hypothesize that polar binder groups, specifically the *carboxyl* moiety, interact strongly with sodium sulfide and short-chain sodium polysulfides, as compared to traditional binders. Such binder-cathode interactions are first predicted computationally in room-temperature NaSBs, then confirmed experimentally using polyacrylic acid (PAA) in combination with a short-chain sulfur-based S-PAN cathode. This strategy of exploiting strong carboxyl-polysulfide interactions can be further generalized, as demonstrated by two other carboxyl- and carboxylate-containing binders derived from nature (*i.e.* carboxymethyl cellulose (CMC) and sodium alginate). Carboxyl binder groups were observed to strongly bind short-chain polysulfides generated during sodiation and prevented

4

cathode pulverization even after repetitive expansion cycles. This was also achieved *without*
the need for elemental-doping or altering the morphology of the particulate S-PAN composite,
as the binder-cathode interactions inherently contributed to superior reaction kinetics. Our
system demonstrated excellent compatibility with both carbonate and ether-based electrolyte
solvents, together with electrolyte additives to ensure stable sodium anode strip/plating. Such
engineering of the NaSBs enabled them to deliver exceptional cycling stability over 1000
cycles with high Coulombic efficiencies close to 100%, and a capacity loss of only 0.016%
per cycle.

2. Results and Discussion

2.1. Density functional theory calculations of binder interactions with sodium polysulfide species

We first consider the issue of cathode pulverization due to the large expected volumetric
expansion from sodiation as postulated earlier. The primary role of a binder is to provide good
adhesion between the active material particulates themselves, conductive carbons, and also
with the current collector, as a means to mitigate against the volumetric changes concomitant
with cycling. However, an effective *bi-functional* binder could also deliver additional benefits
such as preferential binding with the various species and intermediates evolved during
charge/discharge cycling. In NaSBs, the final discharge product, sodium sulfide (Na_2S), is
ionic in nature and highly polar.[26,45] As such, a binder with strong polar character could be
expected to experience stronger binding interactions with Na_2S and other ionic sodium
polysulfides produced during the discharge phase. The most commonly used cathode binder
polyvinylidene difluoride (PVDF) consists of $(CH_2CF_2)_n$ monomer units, and is also
electrically insulating. Although the C–F bond itself is highly polar with a dipole moment of δ
= 1.4 D,[54] PVDF can adopt non-polar conformations (*e.g.* α and ε phases) as a result of their
dipole orientation,[55,56] potentially weakening its bonding with the discharge products. In

comparison, the carboxyl (–COOH) functionality in PAA comprises two strong dipoles, with the carbonyl (C=O) and hydroxyl (O–H) bonds displaying average dipole moments of 2.3 D and 1.5 D respectively.[54] The uncharacteristically strong dipole moment of the carbonyl moiety arises from sp^2-hybridisation of the highly electronegative oxygen atom, suggestive of the pivotal role it could play in its bonding interactions with polar discharge products.

Based on this hypothesis, computational simulations were performed to understand the molecular-level interactions between binder functionalities and the discharge products of the cathode. Using density functional theory calculations, the interactions between the polymers and one sodium sulfide or short-chain polysulfide molecule are simulated (Figure 1). We noted in all cases that bonding interactions could occur through one or both sodium atoms, but not through sulfur. Sodium atoms bonded directly with the most electronegative atoms present in the binder (fluorine in PVDF or oxygen in PAA), while similar electronegative groups further along the chain were found to orientate away from sulfur as a result of their dipole alignments. Such bonding could be anticipated with the more electropositive sodium coordinating with the lone electron pairs on fluorine/oxygen, akin to the bonding between a Lewis acid and base. A close inspection also revealed that with PVDF, only a maximum of two such coordinating bonds could exist between sodium sulfide/polysulfide and the polymer. Conversely with PAA, up to three coordination bonds could be formed with each sodium sulfide or polysulfide molecule. Furthermore, sodium was observed to bind preferentially to the carbonyl oxygen atoms in PAA, in agreement with its strong polar character as we had postulated. Higher adsorption binding energies were therefore obtained between PAA and sodium sulfide, and all other sodium polysulfide species produced during discharge, for example: at 2.02 eV for the Na_2S–PAA interaction *vs*. 1.20 eV for Na_2S–PVDF (Figure 1e). The strong O--Na coordination bond in PAA could also imply that the geminal Na–S bond of the sulfide species becomes easier to break, potentially leading to improvement in reaction

6

kinetics. Also, strong interactions with the carboxyl group would act as a chemical trap *if any*

soluble polysulfides were to inadvertently form during cycling. Next, we proceeded to

experimentally test the effects of these binder interactions in NaSBs, using a sulfurized carbon

composite containing only short-chain sulfur species as active material.
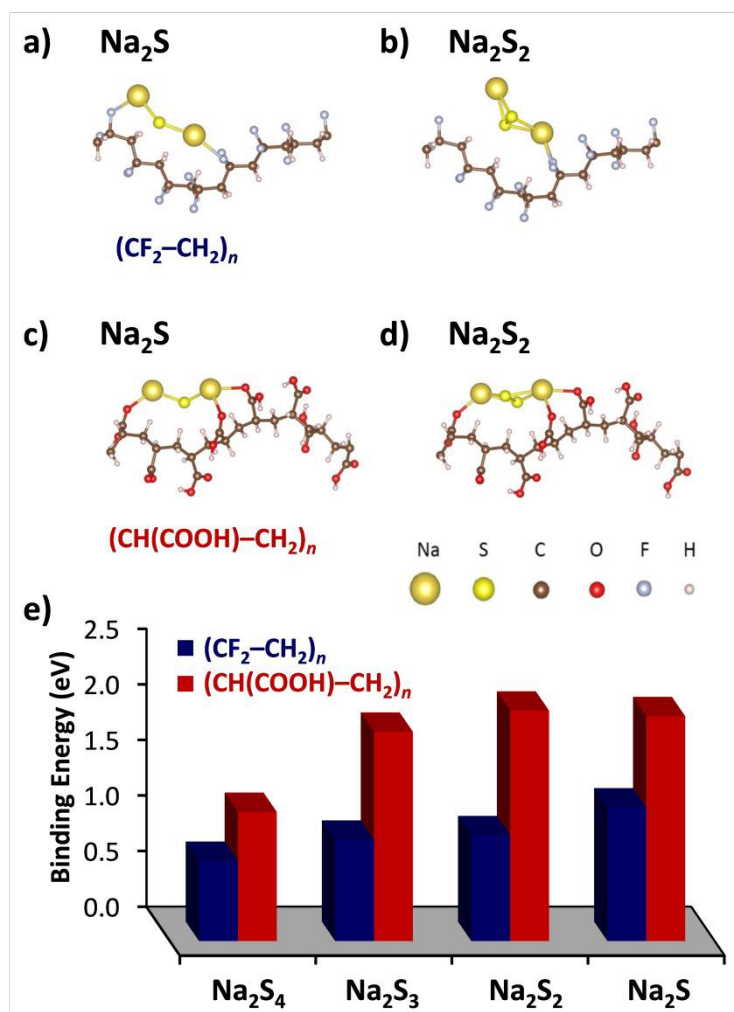

Fig. 1 Density functional theory calculations. Optimised binding configurations of the NaSB discharge product and intermediates with **a,b)** polyvinylidene difluoride $(CF_2–CH_2)_n$, and **c,d)** polyacrylic acid $(CH(COOH)–CH_2)_n$. Each polymer is constructed with eight repeating units in a unit cell. The polymer is repeating along the chain axis. Binding configurations of the polymers with other short-chain sodium polysulfides, Na_2S_3 and Na_2S_4, are available in the Supplementary Information. **e)** Tabulated binding energies of sodium sulfide and short-chain sodium polysulfides with the two binder structures.

2.2. Covalently-bound sulfur in a sulfurized carbon composite

When elemental sulfur (*i.e.* cyclo-octasulfur, S_8) is used as a cathode, it typically results in rapid capacity loss from dissolution of long-chain polysulfide intermediates (Na_2S_x, where $4 < x \leq 8$) and the resultant parasitic shuttle effect. Instead, this issue may simply be eliminated by using insoluble short-chain sulfur that is covalently bonded to the composite structure. Briefly, sulfurized polyacrylonitrile (S-PAN) was synthesized by heating a mixture of elemental sulfur and polyacrylonitrile polymer in an argon-filled tube furnace at 450 °C for 6 hours (see Methods for details). The properties of as-synthesized S-PAN and its chemical structure are investigated herein using a combination of characterization techniques.

Fourier-transform infrared spectroscopy (FTIR) firstly demonstrates the successful cyclization of the PAN precursor[57,58] to S-PAN.[37,59,60] Figure 2a illustrates the loss of both nitrile (C≡N) and methylene CH_2 peaks in PAN. This occurs with a portion of the sulfur acting as oxidant during cyclization, releasing H_2S gas upon reaction with the methylene groups. During this process, sulfur chains also become embedded within the cyclized structure as short-chains (S_{2-4}).[60,61] Any unreacted sulfur is subsequently removed by the carrier gas. As a result, new peaks appear due to the presence of sulfur: S–S stretching and S–S ring breathing at *ca*. 510 cm^{-1} and 930 cm^{-1} respectively, with the absorption at 670 cm^{-1} indicative of new C–S bonding (Figure 2b). Additional strong C=N and C=C bands confirm the cyclization in forming a conjugated pyridine-like backbone (Figure 2h). Despite being bonded directly to the carbon structure, the sulfur content remains high at over 41 wt.% of the composite based on elemental combustion analysis (Table S1). In addition to FTIR spectroscopy, X-ray photoelectron spectroscopy (XPS) was used in determining the surface composition of S-PAN. In Figure 2f, the carbon-1s spectrum revealed a main sp^2-carbon peak at *ca*. 284.4 eV corresponding to a primary graphitic carbon structure, while a second broad peak around 286.2 eV arises from both C–S and C–N species.[60] A further peak close to 288 eV is indicative of sp^2-hybridised C=N bonding. The sulfur-2p spectrum in Figure 2g reveals

three forms of sulfur, with the main $2p_{3/2}$ peak at 163.5 eV characteristic for S–S bonding.

The presence of C–S bonds at a lower binding energy of 161.2 eV confirmed direct covalent

bonding between sulfur and the carbon backbone.[60,61] Contribution of other oxidized species

such as sulfites at 167.5 eV was negligible in comparison.[62]
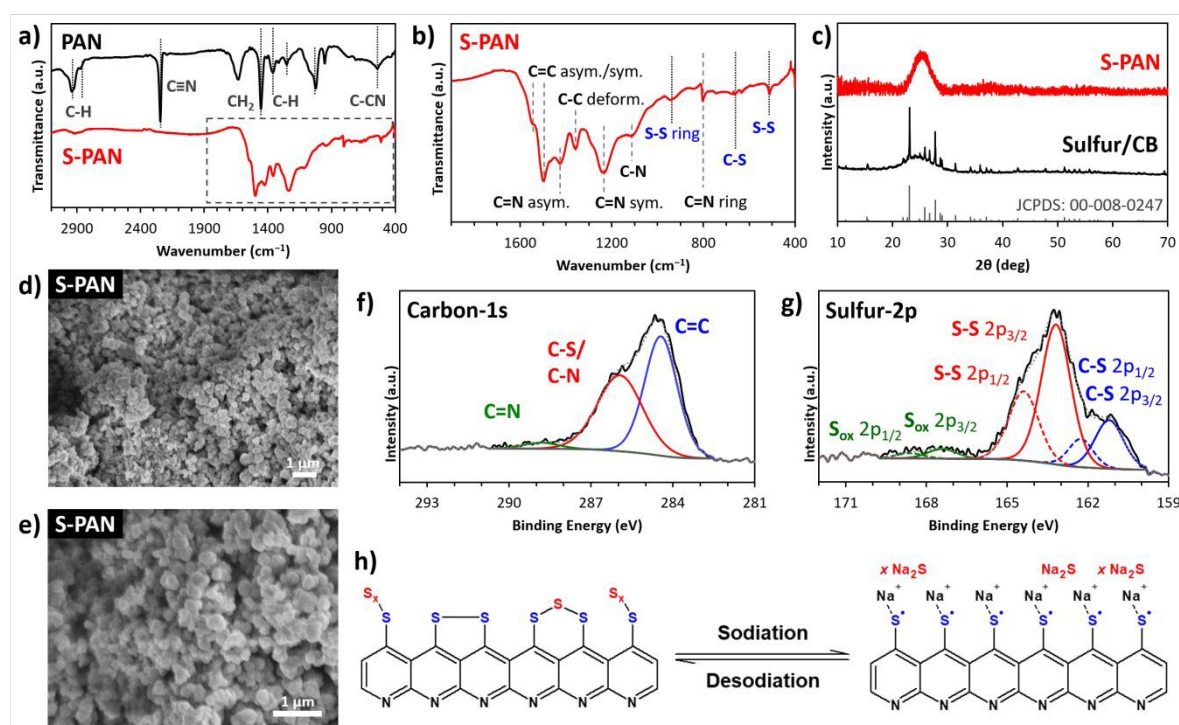

Fig. 2 Structure and morphology of sulfurized polyacrylonitrile (S-PAN) composites. **a)** Fourier-transform infrared (FTIR) spectra of S-PAN and the polyacrylonitrile precursor. **b)** Enlarged FTIR fingerprint region of the S-PAN composite with peak assignments. **c)** X-ray diffractograms of the S-PAN composite in comparison to elemental S_8 sulfur melt-diffused with carbon black. The standard diffraction pattern of orthorhombic sulfur (JCPDS: 00-008-0247) is also provided. **d,e)** Scanning electron micrographs of S-PAN particulates at varying magnifications. High resolution **f)** carbon-1s and **g)** sulfur-2p core-level X-ray photoelectron spectra. **h)** Schematic illustration of sulfur-bonding modes in S-PAN with the corresponding sodiation/de-sodiation reaction.

We also established the lack of residual elemental sulfur in the composite, with X-ray

diffraction (XRD) data showing only a broad (002) peak at approximately 26° from the

graphitic carbon backbone in Figure 2c, indicating the *absence* of elemental sulfur.[37,59,63] This

is contrasted to common carbon black melt-infused with elemental sulfur displaying the diffraction pattern of orthorhombic sulfur (JCPDS: 00-008-0247). Thermogravimetric analysis (TGA) also corroborated with our XRD observations where the main weight loss for elemental sulfur occurred from about 180 °C (Figure S1), whereas the S-PAN composite showed high thermal stability of the sulfur species above 550 °C. Subsequent characterization by time-of-flight secondary ion mass spectrometry (TOF-SIMS, Figure S9) also confirmed bonding between carbon and sulfur fragments, and identified the vast majority of sulfur species to exist as short chains (S_{2-4}).[59] Hence, all sulfur present are covalently bonded to the carbon backbone and stabilized as short-chain species.[37,38,60,64] Finally, the morphology of S-PAN was observed as discrete globular particles approximately 200-300 μm in diameter, and devoid of free unbound sulfur (Figure 2d,e).

As the composite is of a particulate morphology, it is employed as-synthesized without further processing, unlike previous S-PAN cathodes in NaSBs which required either electrospinning[36,37] or compression into a porous foam cathode.[38] Therefore, conventional slurry preparation and roll-to-roll processing can be engaged for cathode assembly. Moreover, as-synthesized S-PAN is a simple two-component composite comprising readily-available precursor materials; sulfur, and the common acrylonitrile polymer with sizable global production exceeding a million tons annually.[65] In our case, we were further able to employ particulate S-PAN *without* a need for chemical-doping (*e.g.* Se, Te, or I) as a recent approach to improve its reaction kinetics in NaSBs.[41-44]

We next explored the sodiation mechanisms of S-PAN in the NaSB system. From XRD in Figure 3a, the pristine cathode displayed only a broad graphitic carbon peak as expected, similar to the pure composite. However, on discharge to 0.6 V *vs*. Na/Na+, we observed the formation of a new peak at *ca*. 39° corresponding to the primary (220) facet of sodium sulfide, Na_2S (JCPDS card: 00-023-0441).[66] This peak disappeared on re-charging to 2.6 V *vs*. Na/Na+. The above observations repeated in successive charge/discharge cycles,

independent of the cathode binder (Figure S2). Broad peaks also likely indicate small crystallites that are well-dispersed throughout composite. Raman spectroscopy provided further evidence for the formation of Na_2S as the discharge product. Other than the D (disorder) and G (graphitic) bands from the carbon structure (Figure 3b,c),[37] cathodes in the discharged state showed a main peak at 596 cm^{-1} and several smaller peaks at 460, 679, 737, and 806 cm^{-1} due to Na_2S.[67] It was also noted that these sodium sulfide peaks were slightly more intense in the PAA-based cathodes compared to their PVDF-based counterparts (Figure S3). Subsequent re-charging resulted in the disappearance of the Na_2S signals, and regeneration of the characteristic S–S signal at 477 cm^{-1}, stretching of S–S ring structures at 925 cm^{-1}, and C–S stretching at 175 and 806 cm^{-1}.[36,37,60,61,63,64]
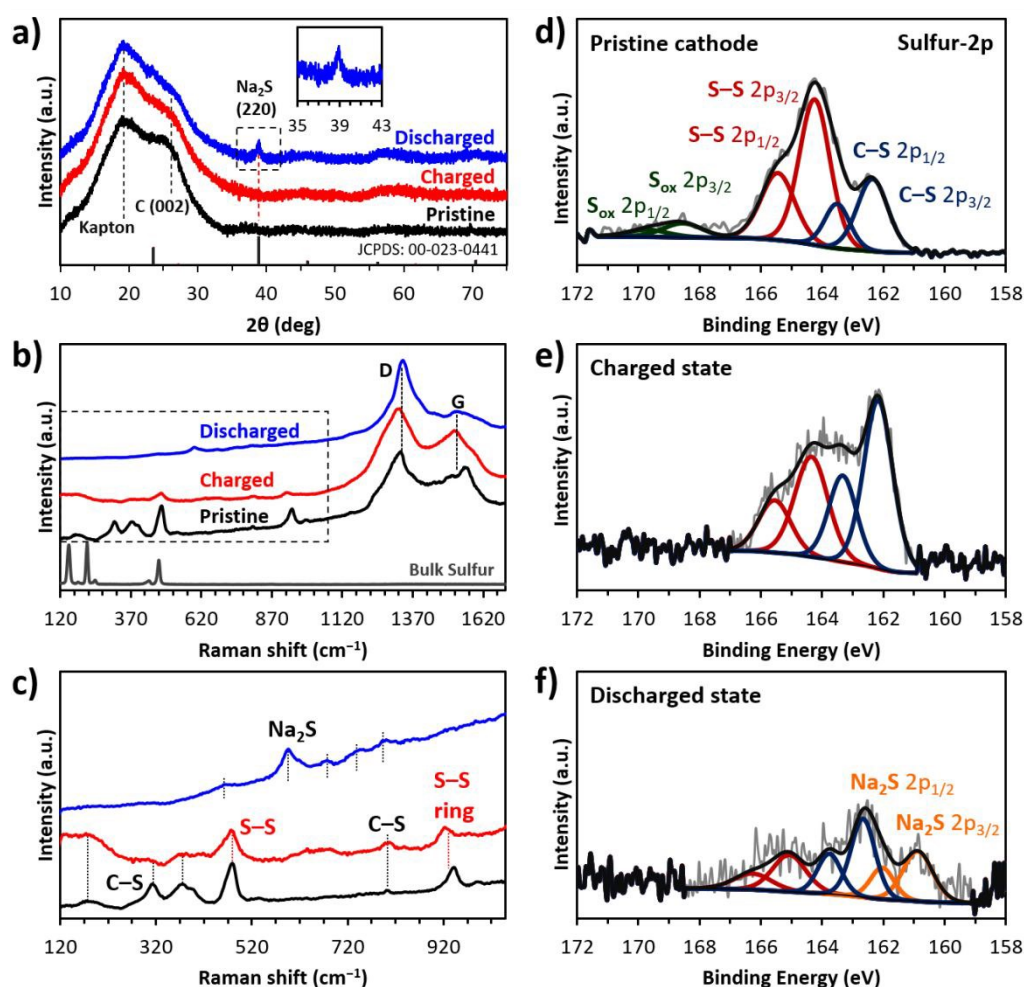

Fig. 3 Sodiation/desodiation of cycled S-PAN composite cathodes, after discharge and subsequent re-charge. **a)** X-ray diffractograms of the cathodes; inset figure for the (220)

reflection of sodium sulfide. The standard diffraction pattern of sodium sulfide, Na_2S (JCPDS 00-023-0441) is also provided. **b)** Raman spectra of cycled cathodes with elemental sulfur for reference. **c)** Enlarged image of the denoted region in b) shown with expanded intensity scales. **d-f)** Sulfur-2p X-ray photoelectron spectra of cathodes in the pristine, discharged, and re-charged states. Data shown for cathodes containing polyacrylic acid binder. Further characterization data for additional cathode binders available in the Supplementary Information.

Similar to the S-2p XPS spectrum of pure S-PAN, it was determined in the pristine cathode that the majority of sulfur originates from S–S species with its $2p_{3/2}$ peak at 164.2 eV,[60,61,68] followed by C–S bonds (Figure 3d and S4). The slight upshift in overall binding energy compared to pure S-PAN is logically attributed to the cathode environment with the presence of electronegative groups from the binder. Upon full discharge to 0.6 V *vs*. Na/Na^+, the intensities of the S–S peaks become diminished.[62] More importantly, we witnessed the formation of a new pair of peaks at lower binding energies, with the $2p_{3/2}$ signal of sodium sulfide appearing at 160.8 eV (Figure 3f).[69] It was also noted that a small amount of C–S species remain, as this terminal bond is sodiated but otherwise uncleaved, similar to the S-PAN lithiation mechanism.[61,62] This was also noted from FTIR spectra, as suggested from the slight weakening of the bond in forming $C–S–Na^+$ species (Figure S8b). Corroborating with Raman spectroscopy on the recharge cycle, the Na_2S signals disappeared, along with the recovery of both S–S and C–S species (Figure 3e).[60] The carbon-1s spectra further revealed the formation of a small amount of sodiated carbon, and also the presence of carbonate-based species above 291 eV attributed to carbonate-based electrolyte decomposition in developing a thin SEI (Figure S5),[12] in line with observations from FTIR spectroscopy (Figure S7,S8). These processes are known to occur during the first discharge and contribute to the irreversible initial capacity typically observed. Finally, TOF-SIMS measurements revealed that the vast majority of sulfur species remained as short-chain fragments after cycling: (S_x, where $2 \leq x \leq 4$), although we noted that the PVDF-based cathode also contained a minute

12

amount (<0.2%) of longer chains (Figure S9). Following the scheme in Figure 2h, XRD, XPS and Raman spectroscopy are in agreement with Na_2S being formed as the main discharge product, and together with FTIR spectroscopy, confirmed regeneration of the covalent sulfurized carbon structure on re-charge. This confirms that the reaction mechanism remains the same in both binder environments, and good reversibility of the electrochemical reaction was also noted.

2.3. Binder effects on the electrochemical sodiation/desodiation of S-PAN

With elucidation of the S-PAN sodiation mechanism and its discharge product, we proceeded to investigate our hypothesis of binder-cathode interactions based on the DFT simulation results. Given that the most basic function of a binder is to maintain good structural integrity and inter-particle adhesion, electron microscopy was first employed to study the differences between carboxyl-containing PAA and traditional PVDF post-cycling. Figure 4 illustrates the variation in morphologies of the two cathode binders which begin to emerge even during the early cycles. While the scanning electron microscopy (SEM) images for cycled PAA-based cathodes (Figure 4a,c) displayed a uniform particle distribution, PVDF-based cathodes in the discharged states exhibited large cracks over 2-3 μm wide (Figure 4b,d) as denoted by red arrows. These areas also corresponded to poorly sodiated regions as seen from the energy dispersive X-ray (EDX) maps for the Na Kα line. Some crevices continued to exist after re-charge (Figure 4f,h), suggesting poor binding interactions between PVDF and the S-PAN composite as a result of volume expansion during the prior discharge cycle. Gradual detachment of active material would follow, leading to incomplete conversion reactions, and could have led to a negligible amount of long-chain intermediates detected earlier. This is opposed to the PAA-based cathode which demonstrated a consistent spatial distribution of sodium, and was able to maintain its structure despite the large volumetric expansion expected from NaSB systems.
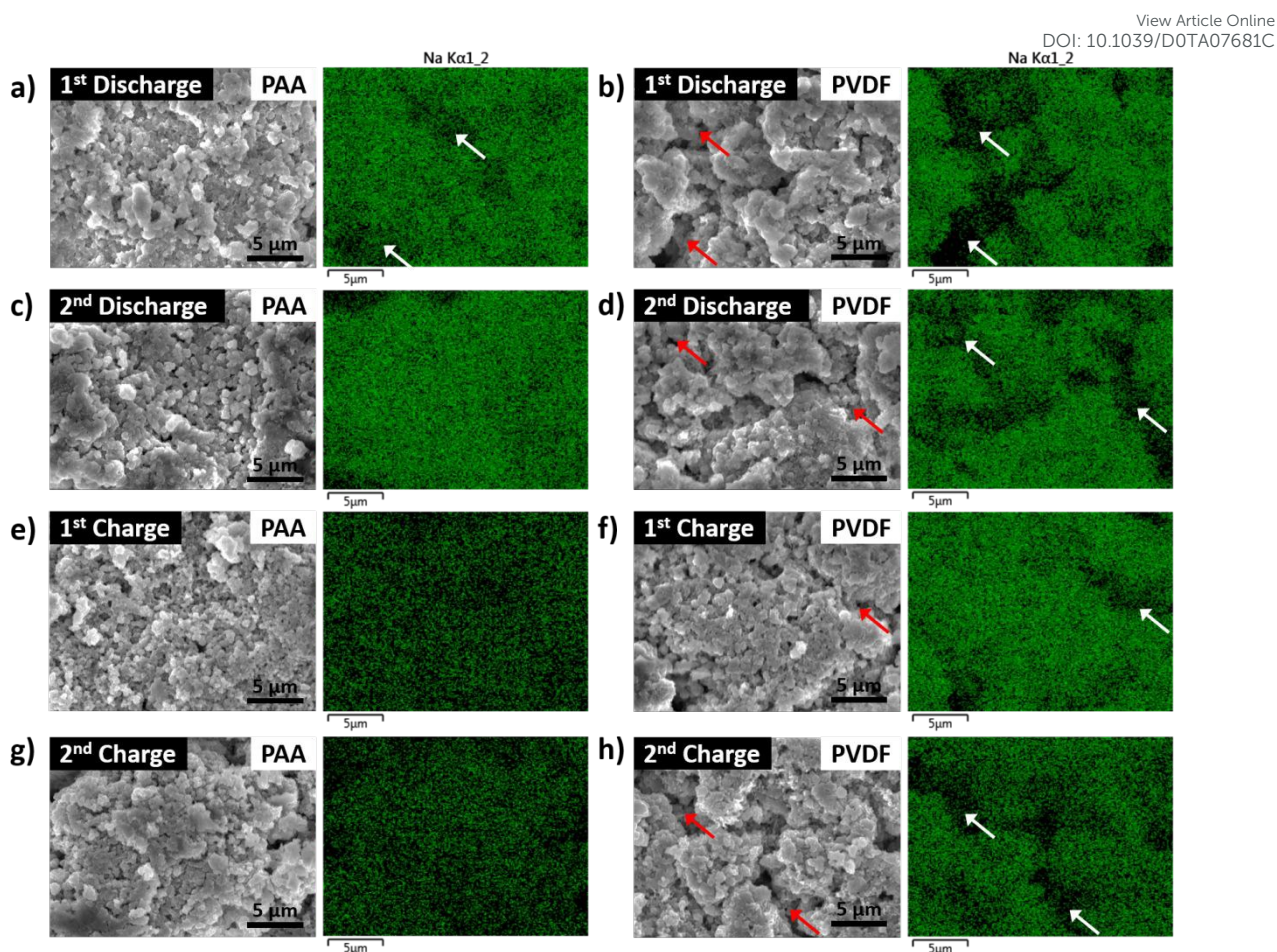
Fig. 4 Scanning electron micrographs of cycled S-PAN cathodes and their corresponding sodium elemental maps by energy dispersive X-ray spectroscopy, for cathodes containing **(a,c,e,g)** PAA binder (left panel) and **(b,d,f,h)** PVDF binder (right panel). Red and white arrows indicate void spaces and regions with lower sodium content, respectively. Elemental maps of other elements are available in the Supplementary Information.

In addition to physico-mechanical properties of the binder, kinetic effects resulting from binder-cathode interactions were examined next. From Figure 5, cyclic voltammetry (CV) displayed prominent differences in the electrochemistry of the cathodes prepared from the binders, shedding light on the interesting differences in their sodiation/desodiation processes. At slow scan rates, two sets of redox peaks were observed for S-PAN (Figure S15), indicating a two-step multi-phase reaction. Starting at the fully charged state, sulfur chains first undergo a $2Na^+/2e^-$ process to form short-chain sodium polysulfide intermediates, which is known to occur at $\sim$2.0 V vs. Na/Na$^+$,[22] followed by further sodiation at 1.3 V to give Na$_2$S

as the final discharge product.[44] During the charging process, sodium sulfide is first converted back to the polysulfide intermediate at *ca*. 1.85 V, then bonding to the composite in the fully charged state, above 2.2 V *vs*. Na/Na$^+$.

$$\text{Equation 1:} \quad S_x \ \rightleftharpoons \ Na_2S_x \ \rightleftharpoons \ x\,Na_2S \quad, \quad \text{where } 2 \leq x \leq 4$$
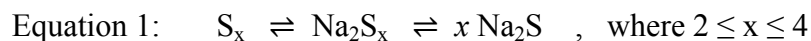
At a slow scan rate of 0.05 mV s^{-1}, both PAA- and PVDF-based cathodes displayed similar sodiation/desodiation mechanisms, except the second anodic peak at *ca*. 2.2 V that appeared slightly diminished in the PVDF cathode (Figure S15b). This indicates that the initial reaction mechanism is similar regardless of binder environment, as one would expect for the same active material.
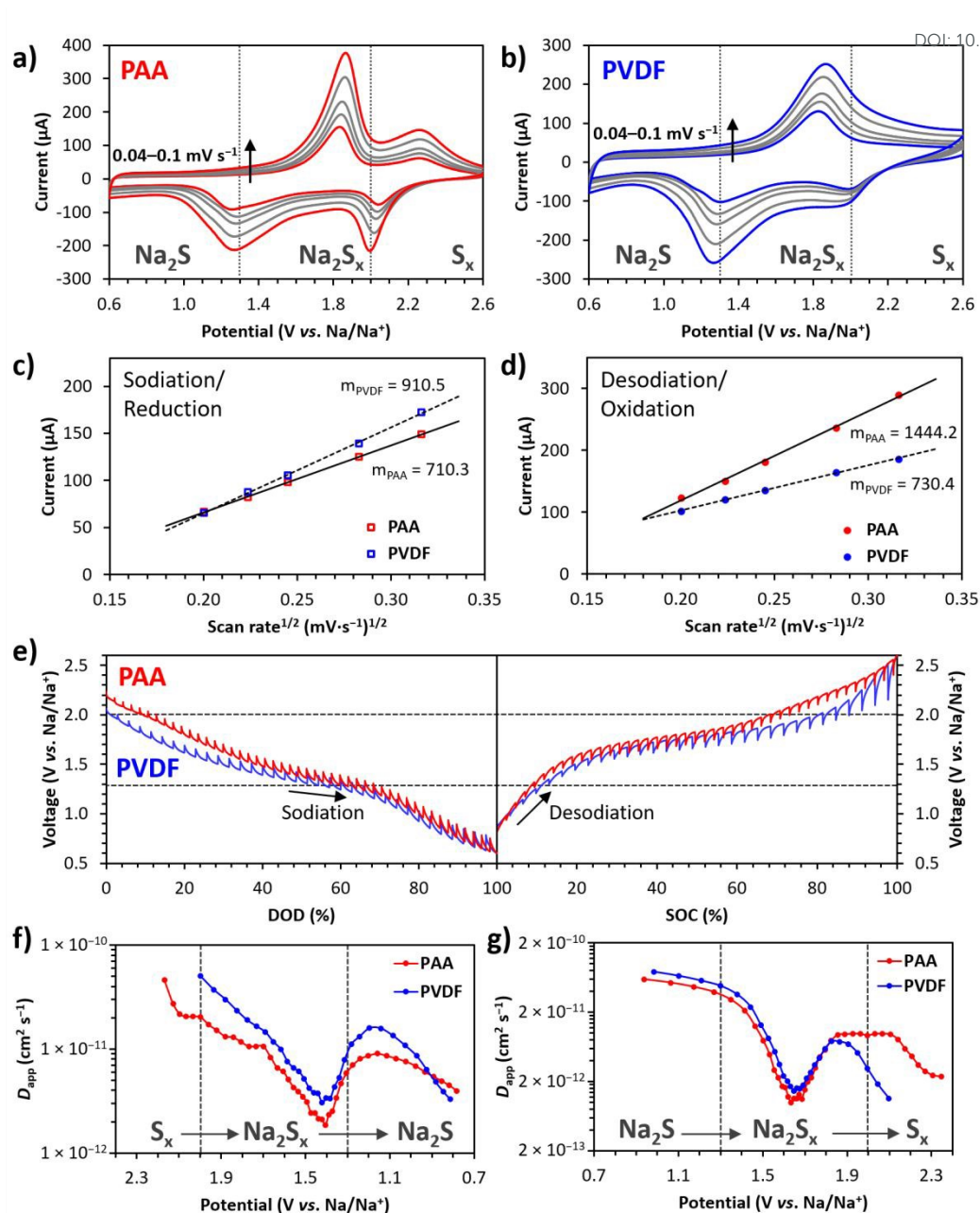
Fig. 5 Cyclic voltammograms of S-PAN cathodes with **a)** PAA binder *versus* **b)** PVDF binder at varying scan rates. Plots of the **c)** cathodic and **d)** anodic peak currents versus the square root of the voltammetric scan rate for PAA (solid lines) and PVDF (dotted lines) cathodes. **e)** Galvanostatic intermittent titration technique (GITT) analysis of S-PAN cathodes. Conditions: 5 min galvanostatic pulses at 0.2 C, followed by 2 h relaxation times. Apparent diffusion coefficients as a function of cell potential for the **f)** discharge/sodiation and **g)** charge/desodiation processes.

In addition to the synthetic PAA binder, we further test our theory on the advantageous binding interactions between carboxyl-groups with polysulfide intermediates and the discharge product, using two additional carboxyl- and carboxylate-containing binders derived from natural products (*i.e.* carboxymethyl cellulose (CMC) and sodium alginate). CMC is a derivative of plant-based cellulose consisting of β-linked glucopyranose substituted with carboxymethyl groups. Sodium alginate is a polysaccharide consisting of β-D-mannuronic acid and α-L-guluronic acid residues partially substituted with carboxylate side groups, obtained from alginic acid present in marine algae and seaweed.[51,52] Cathodes produced from both binders also provided similar voltammetric waves in agreement with the PAA cathode (Figure S15c,d).

At higher scan rates above 0.1 mV s^{-1} however, voltammograms begin to diverge depending on binder choice (Figure 5a,b). Enhanced peak currents and sharp peak-shapes were seen for all carboxyl-containing binders (Figure S16) indicating fast electrode kinetics,[70] especially the cathodic peak at 2.0 V and the anodic peak at 1.85 V *vs*. Na/Na$^+$. Contrastingly, the PVDF-based cathode exhibited sluggish kinetics with a broadened anodic wave at 1.85 V (Figure 5b). Furthermore, reduction of sulfur at 2.0 V became noticeably diminished, while Na_2S_x oxidation at 2.2 V disappeared completely. Based on the evolution of peak currents with scan rate, the Na$^+$ ion diffusion coefficients can be derived. For the reduction process at 1.3 V, the apparent diffusion is only slightly higher in the PVDF cathode compared with PAA (Figure 5c), but otherwise comparable with the other carboxyl binders (Figure S17). This could be attributed to the slow initial sodiation of sulfur in the PVDF environment (seen from the diminished peak at 2.0 V). Thus, a higher overpotential (*i.e.* more cathodic potential) is required to drive the reduction process, resulting in a larger cathodic current observed at 1.3 V.

For the anodic reaction at 1.85 V corresponding to the conversion of Na_2S back to polysulfide (Figure 5d), the apparent Na$^+$ ion diffusion coefficients in carboxyl-binder

environments are more than four times that of PVDF-based NaSBs (Figure S17). A double

logarithmic plot of current *vs*. scan rate also reveals the dominant mode of mass transfer.

From the Randles–Ševćik equation based on semi-infinite diffusion, the double logarithmic

plot is expected to yield a gradient of 0.5.[70] This value can however vary up to 1, which

describes an electrochemical reaction for adsorbed or surface-bound species. Intermediate

values between 0.5 and 1 are not uncommon for mixed diffusion and surface-type reactions,

particularly with S-PAN composites where sodiation occurs on surface-bound S–S species.[43]

Focusing on the anodic process at 1.85 V, values close to 0.9 were obtained in all three

carboxyl-containing cathodes, signifying fast reaction kinetics arising from rapid Na^+ ion

transfer, as compared to the 0.6 value for the PVDF cathode functioning predominantly on

semi-infinite diffusion, not augmented by the surrounding binder environment (Figure S19).

Hence, CV analyses show obvious kinetic enhancements for the sodiation/de-sodiation of S-

PAN in the presence of carboxyl-binders.

We further performed analysis by the galvanostatic intermittent titration technique

(GITT) to acquire kinetic information of the sodiation and desodiation mechanisms.[43,44] While

the apparent diffusion coefficients of all binders were noted to range between similar orders

of magnitude (Figure S20), two major mechanistic differences were observed with PVDF as

compared to the other carboxyl-containing binders. Firstly, the initial discharge potential for

the PAA cathode begins at a higher potential of 2.2 V *vs*. Na/Na^+ at 0% depth-of-discharge

(DOD) (Figure 5e), equivalent to the onset potential of the same sulfur-to-polysulfide

transition seen from CV. This was similarly observed for both CMC and alginate binders,

with nearly identical discharge curves (Figure S20). The discharge of PVDF-based cathodes

however starts at a lower potential of 2.0 V, corroborating with evidence from CV earlier in

suggesting that a greater overpotential is required to drive the reduction of sulfur in S-PAN,

when in the absence of a carboxyl-binder environment. Secondly, close inspection of the

charge curves of all four cathodes reveals the main dissimilarity arising at *ca*. 65-100% state-

of-charge (SOC) in the PVDF cathode, versus those of the other carboxyl binders (Figure 5e and S20b). This region represents the conversion of Na_2S_x back to sulfur. In the duration of each relaxation interval at high SOC, the PVDF cathode was noted to experience increasingly larger losses in cell potential as the system continually reverted to lower oxidative states, thus demonstrating a difficulty for the desodiation process to proceed from Na_2S_x polysulfides back to the original sulfur species. As such, GITT results agree well with CV data showing that the redox conversion between covalent sulfur and sodium polysulfide is greatly enhanced in the presence of carboxyl binders, but significantly hindered in the less polar PVDF environment.

In terms of diffusion rates, GITT achieved a more precise trend for Na^+ ion diffusion rates as a function of cell potential, compared to CV where kinetics of the sulfur-polysulfide redox couple (2.0–2.2 V vs. Na/Na$^+$) could not be studied in the PVDF cathode due to their disappearance at fast scan rates. In the sodiation process, all carboxyl-containing cathodes displayed comparable trends for Na^+ ion diffusion, from a high apparent diffusion coefficient (D_{app}) of 5×10^{-11} cm^2 s^{-1} upon initial discharge at 2.2 V (Figure 5f and S20c). PVDF-based cathodes could only begin discharging from a lower potential, which likely resulted in the slightly higher calculated coefficients as the reaction proceeded more efficiently at greater cathodic overpotential.

More interestingly for the desodiation process, the apparent Na^+ diffusion in all cathodes followed a typical two-phase profile,[34,41,43] gradually decreasing from the fully discharged state (Figure 5g). Comparable coefficient values around 6×10^{-11} cm^2 s^{-1} for all cathodes indicated similar kinetics for the first oxidation process from Na_2S to Na_2S_x (Figure S20d). In the subsequent polysulfide conversion to sulfur, a maximum was reached around 1.85 V for the PVDF cathode but which decreased rapidly thereafter (Figure 5g and S20d). This maximum occurred before the required thermodynamic potential of ~2.0 V vs. Na/Na$^+$ to efficiently oxidize short-chain polysulfides ($e.g.$ Na_2S_2, Na_2S_3) back to sulfur.[22] Carboxyl-

containing cathodes however experienced faster Na^+ diffusion rates, maintaining a plateau up till 2.15 V for enhanced kinetic conversion. Consequently, the collective data suggests that the $S_x \rightleftharpoons Na_2S_x$ conversion is the main rate-limiting step of the overall reaction. Fast kinetics is observed in the presence of carboxyl-binders, whereas a conventional fluoropolymer binder impeded the reaction progress.

2.4. Effects of carboxyl-containing binders on long-term battery cycling

With the insight into both physico-mechanical and electrochemical influences that the binders exerted on the NaSB cathodes, we carried out further long-term battery cycling tests. Figure 6a and 6b illustrate the evolution of galvanostatic charge/discharge curves for both the carboxyl-based PAA cathode and PVDF cathode, between 0.6 V and 2.6 V vs. Na/Na^+. The initial discharge took place as a single sloping plateau at low potential, contributing an irreversible capacity due to carbonate-electrolyte decomposition in forming the SEI layer,[12,43] in line with our earlier XPS findings. With continued cycling, we noted an interesting observation for the PAA cathode (Figure 6a): a sloping double-plateau charge/discharge profile gradually developed with increasing cycle number. For the charging process, the first plateau occurred at ca. 1.8 V and the second at about 2.2 V vs. Na/Na^+, which corresponds well to the two-phase sodiation/desodiation mechanism seen from CV and GITT. Two-plateau curves were similarly obtained for CMC- and alginate-based cathodes (Figure S23), but was absent in the PVDF system. Instead, the PVDF cathode cycled in Figure 6b displayed only a single slanted plateau at 1.8 V. Furthermore, significant capacity loss quickly followed within the first 10-20 cycles, resulting in a specific capacity below 600 $mAh \cdot g_{(S)}^{-1}$ by the 100th cycle at 0.2 C (1 C = 1673 $mA \cdot g_{(S)}^{-1}$). This is in stark contrast to the PAA-based battery sustaining a high capacity of 1170 $mAh \cdot g_{(S)}^{-1}$ even after 300 cycles at 0.2 C (Figure 6c).
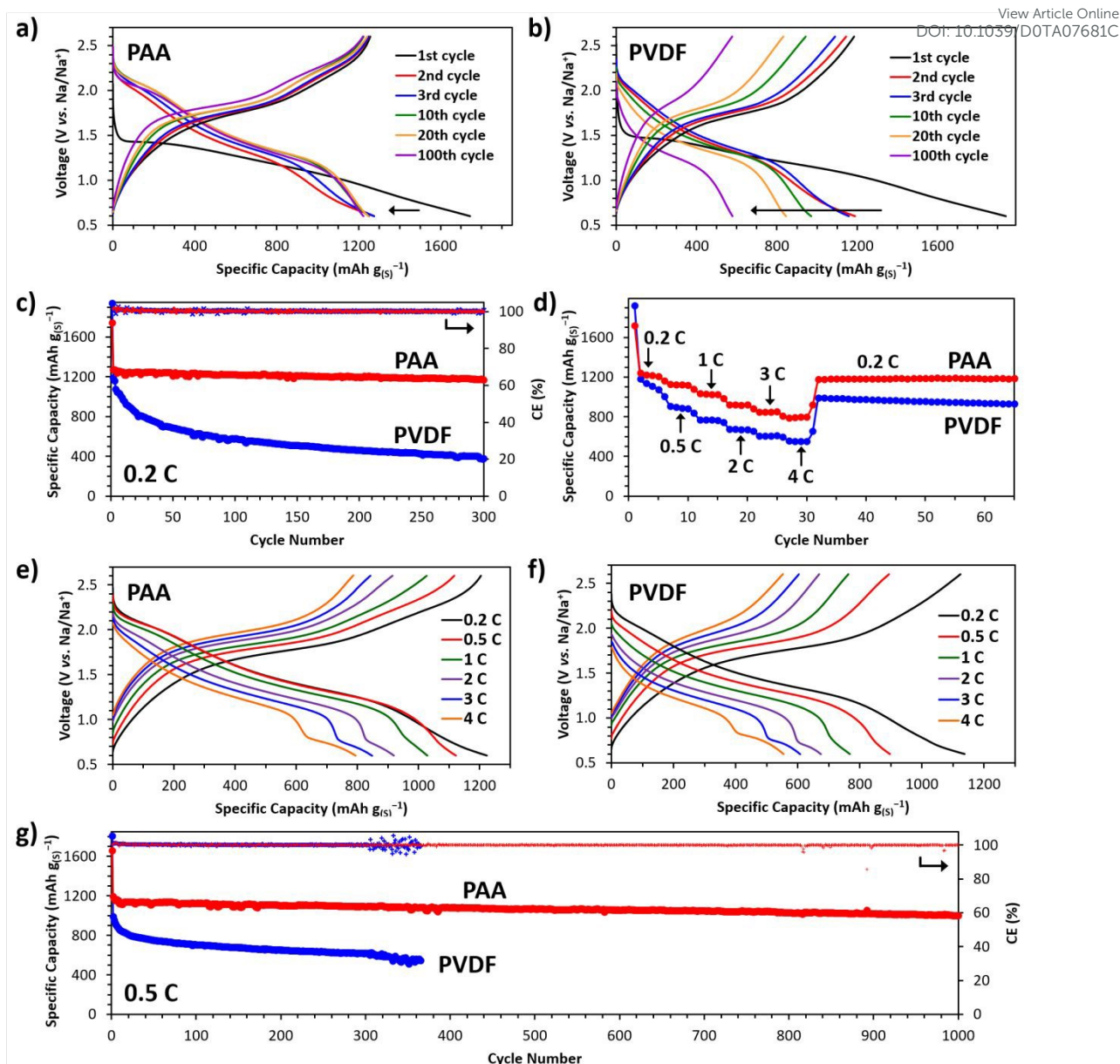
Fig. 6 Galvanostatic charge/discharge profiles for sodium-sulfur cells at 0.2 C, containing S-PAN cathodes with **a)** polyacrylic acid (PAA) *versus* **b)** polyvinylidene fluoride (PVDF) binders. **c)** Cycle performance and Coulombic efficiencies of sodium-sulfur cells at 0.2 C. **d)** Rate performance comparison and galvanostatic charge/discharge profiles for **e)** PAA-based and **f)** PVDF-based cathodes between 0.2 C and 4 C, where 1 C = 1673 mA·$g_{(S)}^{-1}$. **g)** Extended galvanostatic cycling at 0.5 C for S-PAN sodium-sulfur cells.

High rate performance for the PAA-based cathode was also achieved (Figure 6d), with capacities of 1023 mAh·$g_{(S)}^{-1}$, 920 mAh·$g_{(S)}^{-1}$, and 800 mAh·$g_{(S)}^{-1}$ at 1 C, 2 C, and 4 C respectively. Carboxyl-containing CMC and alginate binders also exhibited excellent rate

performances around 950 mAh·g$_{(S)}$$^{-1}$ at 4 C (Figure S23). These were superior to the PVDF-based cathode presenting just 554 mAh·g$_{(S)}$$^{-1}$ at 4 C, due in part to increased charge transfer resistances seen from electrochemical impedance Nyquist spectra after cycling (Figure S22). In addition to carbonate-based electrolytes, our system also demonstrated excellent compatibility with ether-based electrolytes. Particularly, the PAA-based cathode achieved a good rate capability of *ca.* 650 mAh·g$_{(S)}$$^{-1}$ at 4 C with a diglyme-based (diethylene glycol dimethyl ether) electrolyte (Figure S37). This presents potential benefits with ether-based electrolyte systems reported to show greater resistance towards reduction, and are thus able to realize higher initial Coulombic efficiencies due to thinner anode SEIs.[71] Separately, the superior rate performance in both electrolyte systems may allow for fast-charging capabilities in upcoming flexible Na-batteries, where Hu and co-workers have recently postulated the application of S-PAN nanofiber webs as flexible cathodes.[72] This may also be achieved in our system through the use of flexible carbon paper substrates with increased sulfur loads (Figure S38).

Finally, long-term battery cycling showed an exceptional level of performance for the NaSB. At 0.5 C, the PVDF-based cathode again experienced much of its capacity loss within the first tens of cycles, further displaying instability and erratic Coulombic efficiencies after a few hundred cycles; a low specific capacity of just 619 mAh·g$_{(S)}$$^{-1}$ was obtained at the 300[th] cycle (Figure 6e). Post-mortem analysis of the cathode showed partial disintegration of the material after just 50 cycles (Figure S27), along with the formation of a passivating surface film. Instead, the PAA-based cathode delivered an exceedingly stable performance, from an initial capacity of 1195 mAh·g$_{(S)}$$^{-1}$ in the second discharge, to 1000 mAh·g$_{(S)}$$^{-1}$ at the 1000th cycle with Coulombic efficiency close to 100%. This represents a capacity loss of only 0.016% per cycle, compared to 0.13% with the PVDF-based cathode over a shorter 300 cycles. To the best of our knowledge, the S-PAN(PAA) cathode represents one of the best capacity retentions over 1000 discharge cycles for room-temperature NaSBs to date (Table

S10). The gravimetric energy density also reaches as high as 710 Wh/kg$_{composite}$ (details in the Supplementary Information), towards the development of practical NaSB systems.

To verify that the superior performance of NaSBs assembled from the S-PAN(PAA) cathode indeed derives from their synergistic binder-cathode interactions, we conducted extensive tests on all other cell components. The first control was performed using an ultra-high molecular weight PVDF from an alternate source. These prepared cathodes similarly exhibited large initial capacity decays and rate performances inferior to carboxyl-binders, signifying that such negative effects are independent of polymer chain length (Figure S24). Conductive carbon and the binders themselves do not contribute to the measured capacity, nor does the carbonized-PAN composite structure itself (*i.e.* no sodiation of the carbon backbone; Figure S26). These tests also confirmed that carboxylic groups in the binder do not exhibit electrochemical activity within the potential window, unlike speciallly designed redox-active carbonyl, carboxyl or quinonyl compounds in sodium-ion battery systems.[73] A further set of control experiments was also done to determine if the effect of any electrolyte additive could have influenced the observations. In the present study, we employed a combination of both SnCl$_2$,[10,11] and fluoroethylene carbonate (FEC)[13,14] additives in the electrolyte known to form stable intrinsic Na-anode SEIs. Neither additive alone was found to adequately stabilize the sodium anode for our intended long-term cycling, as we observed from symmetric sodium strip/plating studies (Figure S33 and S34). Only a combination of both allowed for stable strip/plating of sodium at low overpotentials over extended durations, thus establishing that these additives acted just on the sodium anode. Moreover, the additives did not improve either capacity or Coulombic efficiency of the NaSBs when added separately to the electrolyte (Figure S35). Lastly, a comparison between PAA and PVDF cathodes in the *absence* of all electrolyte additives supported our earlier findings that PVDF results in a rapid rate of initial capacity decay, while the PAA cathode continued on a much slower decline gradient (Figure S25). As such, electrolyte additives could only help to reduce the long term rate of decline,

but have no effect in preventing large initial capacity losses solely influenced by binder-cathode interactions.

Post-mortem analyses of the electrodes were also performed after cycling. No polysulfide crossover or dissolution was detected, either on the separator or bare sodium anodes even after cycling for up to 200 cycles (Figure S27g and Table S9) in the absence of electrolyte additives, and regardless of cathode-binder. This is due to the covalent nature of the sulfur in S-PAN that is *insoluble* in the electrolyte. Since S-PAN only contains short-chain sulfur bonded to the carbon backbone, soluble long-chain polysulfides could not be detected even after extended cycling. Instead, the issues once again lay only with the PVDF-based cathode.

In the cycled PVDF cathode, we noted a greater density of extensive fractures, some of which were more than 10 μm wide (Figure 7a,b), and running up to several hundred micrometers in length. These fractures developed over time from repetitive volume expansion and contraction cycles as the structure deteriorated from the early stages in Figure 4. Considering their structure-property relationships, the poor capacity retention of PVDF-based cathodes during early cycle life could be fundamentally attributed to the two factors observed earlier: *(1)* poor binding and adhesion of PVDF-based cathode components leading to loss of structural integrity, and *(2)* weak binding interactions between the C–H/C–F functionalities of the polymer and the discharge product/intermediates of the S-PAN composite. The former effect was physically observed by microscopy, and also manifested as a higher charge transfer resistance. At the molecular level, weak binder-cathode interactions in the PVDF system were originally predicted by our computational simulations, and also found to result in inferior reaction kinetics as evidenced by electrochemical characterization.
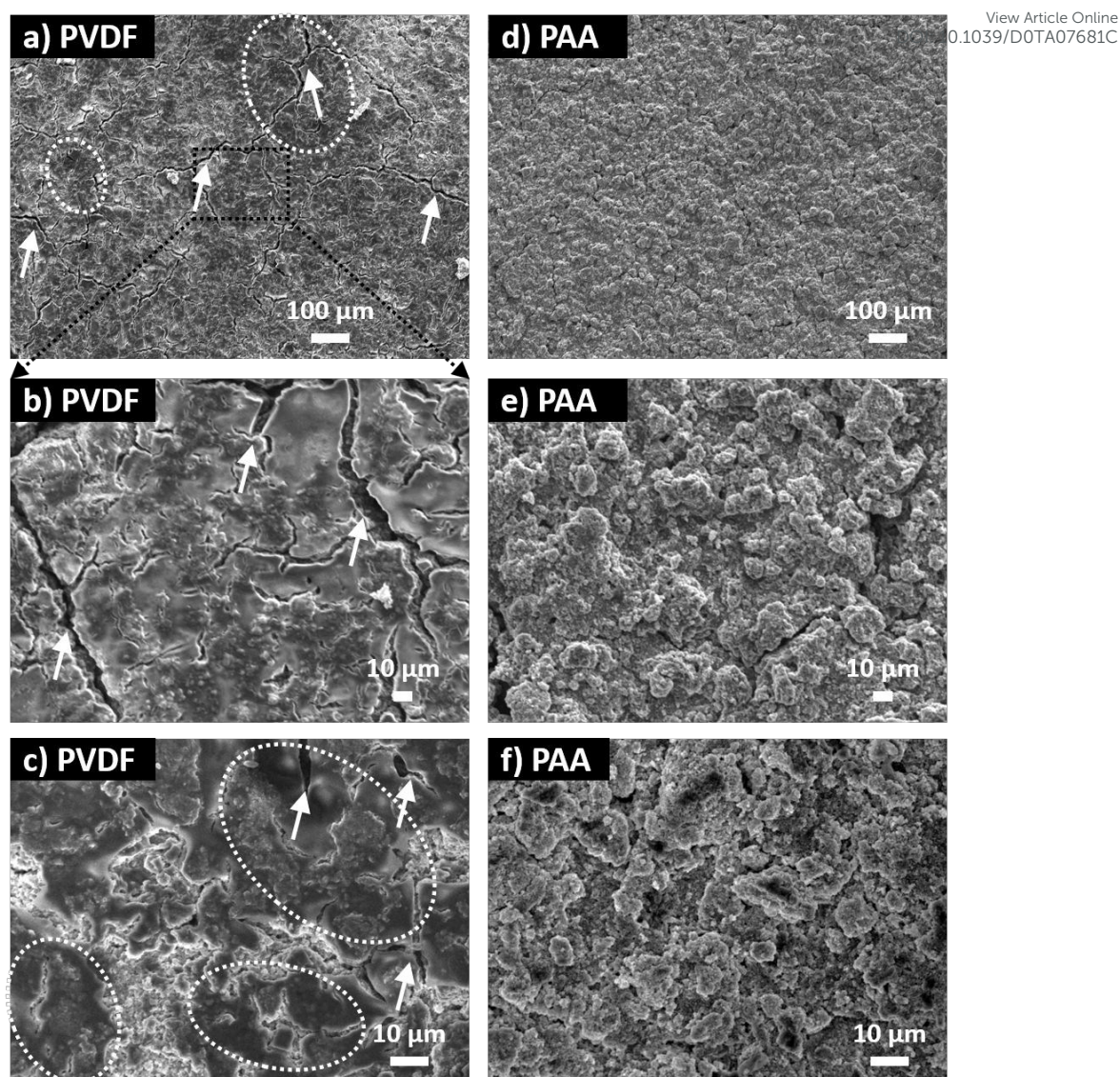
Fig. 7 Post-mortem analysis of the cathode architecture after galvanostatic cycling for 50 cycles, ending in the charged state. SEM images of the **a-c)** PVDF cathode and **d-f)** PAA cathode at varying magnification. Figure b is an enlarged image of the demarcated region in a). Additional higher magnification images of cathode and anode components are available in the Supplementary Information. White arrows indicate large fractures within the cathode; dotted ovals denote regions of lower contrast formed as a surface passivation layer.

Conversely for the PAA-based S-PAN cathode (Figure 7d-f), no large cracks were seen, demonstrating the ability of the carboxyl binder-cathode combination to accommodate the severe volumetric changes associated with NaSB cycling. In the lithium-ion battery system, Yushin and co-workers first reported the high elasticity of PAA allowing for expansion of silicon anodes during lithiation.[74] Aurbach and co-workers later attributed good

structural retention to strong bonding of carboxyl groups in PAA not just with the carbonized structure, but also with surface oxides of the aluminum current collector.[48] In addition to these above arguments however, we further report on the strong interactions between *carboxyl* groups (represented by three separate binders: PAA, CMC, alginate) and the sodiated discharge products and intermediates (*i.e.* sodium sulfide and polysulfides), which led to improved reaction kinetics as we observed for the very first time here in NaSBs.

Moreover, in addition to our observed *(1) physico-mechanical* effects (*i.e.* structural retention *vs.* fractured cathodes) and *(2) electrochemical* effects (*i.e.* fast *vs.* hindered kinetics), closer examination of the cycled cathodes also uncovered *(3)* the slow growth of a non-uniform gel-like film developing only on the surface of the PVDF cathode. Such areas cover the underlying particulate active material (Figure 7c), and appeared as darker regions of lower contrast in the SEM, suggestive of lower electronic conductivity. Additional images of such regions may be found in the Supplementary Information (Figure S27). With a greater number of cycles, almost the entire PVDF cathode surface was found to be covered, after 100 cycles (Figure S29a). Instead, PAA-based cathodes continued to preserve their particulate morphologies throughout, enabling direct contact with the electrolyte and maintaining good wettability. Elemental quantification from EDX in Table S7 indicated this layer to be enriched in both sodium and oxygen (and also fluorine from the PVDF binder). It also contained significantly less sulfur, nitrogen, and carbon *versus* the PAA-based counterpart, thus confirming that the S-PAN composite becomes progressively buried under this surface film. Nonetheless, it was finally determined by XPS depth profiling that this layer consisted primarily of fluorinated carbons together with a carbonate-type species (Figure S31), *i.e.* PVDF binder containing decomposed carbonates, which completely covered the underlying sulfur active material. This was indicated by the strong 688 eV fluorine-1s peak characteristic of the $-CF_2-$ polymer structure,[75] and also C-O and O-C=O bonding in the carbon-1s

spectrum. Consequently, the intensity of these peaks decreased after ion sputtering to reveal the underlying sulfur active material.

The phenomena very likely occurred due to progressive swelling of the PVDF binder in the electrolyte solvent over an extended period.[76] With silicon anodes for example, PVDF was estimated to swell by around 20% after immersion for 40 h in carbonates.[77] We may thus envisage the following situation: during discharge, cathode expansion results in some intake of carbonate solvent together with electrolyte ions. On the charge cycle however, while desodiation leads to contraction of the active particulate composite, weak binder-composite interactions inadvertently lead to the binder associating preferentially with the solvent instead. Successive cycles over the long term would consequently result in the steady build-up of swollen fluorocarbon polymers on the top cathode surface contacting the electrolyte, just as we observed with the gel-like layer. In agreement with our findings for NaSB binder-cathode interactions, Magasinski *et al.* reported that unlike traditional PVDF, PAA exhibited minimal interaction with electrolyte solvents for lithium ion battery anodes.[74] More recently, Shaibani *et al.* also found that the standard practice of wet mixing using pre-dissolved binders for cathode slurries could lead to large portions of the active material becoming encased by the inactive binder,[78] thus reducing the electrochemically-active surface area and limiting electrolyte diffusion. Similar to this concept on active surface areas, we see that for PVDF-based S-PAN cathodes, incompatibility of the PVDF binder with carbonate electrolytes led to swelling over the long-term, reduced electrolyte contact with active material, and eventually contributed towards capacity loss. Despite the identical composite and preparation techniques employed, no such occurrences transpired with the PAA-based cathode, highlighting the vital importance of the binder in NaSBs.

3. Conclusions

In summary, we report that binder-cathode interactions form a critical aspect in the rational design of sodium-sulfur batteries to solve the existing problems of capacity loss from polysulfide dissolution, and structural deterioration due to severe volume expansion. This was achieved in the present study by exploiting the positive interactions between *carboxyl*-containing binders and an S-PAN sulfurized carbon cathode. The issue of polysulfide dissolution is first addressed by eliminating soluble sulfur species from the active material. Any potential formation of soluble polysulfides during battery cycling is then further inhibited, by employing a carboxyl binder to strongly bind discharge products and intermediates and promote their rapid conversion. Furthermore, strong binder interactions with the active material allowed the system to tolerate recurrent volumetric changes. Clear distinctions were therefore observed between PAA and traditional PVDF binders, in terms of both *physico-mechanical* and *electrochemical* effects. PVDF-based cathodes suffered sluggish kinetics during early cycling, and developed structural fractures alongside binder swelling over the longer-term. Conversely, NaSBs based on the PAA-binder S-PAN combination displayed excellent structure retention and enhanced kinetics. Hence, optimization of binder-cathode interactions is a straightforward, yet effective approach for us to push the limits of sodium-sulfur battery technologies towards potential future deployment.

4. Methods

4.1. Materials

Sodium cubes (99.9%), elemental sulfur ($\geq$99.5%), polyacrylic acid (avg. M_W = 450,000), polyacrylonitrile (avg. M_W = 150,000), sodium carboxymethyl cellulose, sodium alginate, polyvinylidene difluoride (avg. M_W = 534,000) were acquired from Sigma Aldrich. A second battery-grade ultra-high molecular weight PVDF binder (avg. M_w = 1.0−1.1 M) was obtained

from Solvay, Belgium. Carbon fiber paper was purchased from AvCarb Material Solutions.

Electrolyte solvents and additives, including sodium perchlorate (≥98.0%), carbon black

(Super P), tin (II) chloride, and anhydrous solvents, fluoroethylene carbonate, ethylene

carbonate, diethyl carbonate, dimethyl carbonate, diethylene glycol dimethyl ether (diglyme)

and tetraethylene glycol dimethyl ether (tetraglyme) were also purchased from Sigma Aldrich.

All electrolyte chemicals were stored and used within an argon atmosphere (H_2O < 0.1 ppm,

O_2 < 1 ppm).

4.2. Synthesis of sulfurized polyacrylonitrile composite

Elemental sulfur powder and the polyacrylonitrile polymer were first mixed by grinding in a

weight ratio of 5:1. The ground mixture was subsequently placed in alumina boats and

transferred to an argon-filled tube furnace (99.99% purity, flow rate of 50 sccm). The furnace

was increased from room temperature at a ramp rate of 10 °C min^{-1}, and further maintained at

450 °C for 6 hours before being allowed to cool naturally, yielding a black particulate

composite. The procedure was repeated for the control sample, carbonized polyacrylonitrile

(cPAN), in the absence of sulfur.

4.3. Materials characterization

Elemental combustion (CHNS) analysis was performed on a Thermo Scientific Flash 2000

analyzer, with samples prepared in tin-foil capsules. Sulphanilamide was used as analytical

standard (Elemental Microanalysis, UK) for calibration prior to each measurement. FTIR

spectroscopy was performed on a Spectrum 2000 instrument (Perkin Elmer) in transmittance

mode. Samples were prepared in a glovebox by grinding and forming a KBr pellet, before

transfer in a sealed vessel. Thermogravimetric analysis was completed on a TA Instruments

Q500 with a temperature ramp of 10 °C min^{-1}, under constant nitrogen gas flow.

Powder X-ray diffraction was completed using a Bruker D8 ADVANCE X-ray

diffractometer using a Cu Kα source at λ = 1.5406 Å. For electrode post-mortem studies, a D8

DISCOVER X-ray diffractometer was used, with a thin polyimide Kapton tape (Caplinq,

Netherland) to protect the sample from atmospheric exposure during measurement. SEM was

done on a JEOL 7600F field emission scanning electron microscope (JEOL, Japan), fitted

with an energy dispersive X-ray detector (Oxford Technologies, UK). Air and moisture

sensitive samples were prepared in an argon-filled glovebox by affixing on conductive copper

tape, before transfer to the loading chamber in an air-tight holder. EDX mapping and

quantification was performed with an accelerating voltage of 10 kV. A Renishaw inVia

confocal Raman microscope was employed for Raman spectroscopy, using a 532 nm

excitation laser in backscattering geometry. Samples were sealed between two quartz slides,

and instrument calibration achieved with a silicon reference. A Thermo-Scientific Theta

Probe spectrometer was used to obtain X-ray photoelectron spectra, with an Al Kα X-ray

source. Relative sensitivity factors were included in the calculation of elemental compositions

and binding energies referenced to the C-1s peak for graphitic carbon.[78] A custom-built XPS-

holder was used to transport samples from an argon-filled glovebox directly to the analysis

chamber without exposure to the environment. Further depth profiling was done with *in-situ*

Ar^+ ion sputtering. TOF-SIMS measurements were obtained with a TOF.SIMS 5 instrument

(IONTOF, Germany) using a Bismuth primary ion beam at 30 keV, over a sample area of 100

× 100 μm.

4.4. Electrochemical characterization

All cathode slurries were prepared using *N*-methyl-2-pyrrolidone (NMP) and casted by

laboratory-scale doctor blades on carbon-coated aluminum foil, typically consisting of 10

wt% of the respective polymer binder (*e.g.* PAA, PVDF, CMC, Na-alginate), 70 wt%

sulfurized polyacrylonitrile active material, and 20 wt% carbon black before drying at 70 °C. In the case of CMC and Na-alginate, the binders were first dissolved as a 5 wt.% aqueous solution before addition to the NMP-based slurry mixture. Particularly for post-mortem spectroscopic analyses, a modified cathode composition of 10:85:5 was employed for binder, composite, and carbon black by weight, respectively. This was done to reduce background interferences from the conductive carbon. The areal mass loading of the S-PAN composite was kept between 1.1–1.8 mg cm^{-2} ($\sim$0.5–0.7 mg$_{(S)}$ cm^{-2}) for experimental consistency. Higher areal mass loads of up to *ca*. 6.5 mg cm^{-2} may also be achieved with a carbon fiber paper cathode, corresponding to a sulfur mass loading of $\sim$2.5 mg$_{(S)}$ cm^{-2}.

Electrochemical testing was performed with 2032-type coin cells assembled in an argon-filled glovebox with the S-PAN composites as the cathode (11.28 mm, 1.0 cm^2). Freshly cleaved sodium blocks (99.9%) were rolled into sheets and cut into circular discs serving as the anode (12.7 mm). A glass fiber membrane (16.2 mm) was filled with 1 M NaClO$_4$ electrolyte (80 µL) in a 1:1 volume mixture of ethylene carbonate (EC) and dimethyl carbonate (DMC) solvent and used as separator, containing 40 mM SnCl$_2$ and 8 vol.% FEC additives unless otherwise stated. As further described in the Supplementary Information, additional control experiments were undertaken containing only SnCl$_2$ or FEC alone, or neither of the two electrolyte additives. For Na//Na symmetric cell testing, two equivalent sodium discs were used with the different electrolyte combinations above.

Galvanostatic charge/discharge cycling was conducted at varying C-rates (1 C = 1673 mA·g^{-1}) using a Neware CT 3008 battery tester, between 0.6 V and 2.6 V *vs*. Na/Na$^+$. Cyclic voltammetry, electrochemical impedance spectroscopy (EIS), and the galvanostatic intermittent titration technique (GITT) were carried out from a Gamry Interface 1000 potentiostat. EIS was performed with a 5 mV alternating current perturbation at open circuit potential, over a frequency range of 1 MHz to 0.01 Hz. GITT was performed by

discharging/charging the cells with 5 min current pulses at 0.2 C, followed by 2 h relaxation intervals.

4.5. Density functional theory (DFT) calculations

The polymer chain of PVDF and PAA are constructed using the Build Polymers function implemented in Materials Studio software suite. Eight repeating units are used for each polymer in a periodic unit cell (the polymer is repeating along the x-direction).[79] The initial structures are first relaxed using the Forcite module with the Dreiding forcefield.[80] Full geometry optimizations with spin-polarization are then performed using DFT within the generalized gradient approximation (GGA) in the form of Perdew, Burke, and Ernzerhof (PBE) exchange-correlation functional[81] implemented in Vienna Ab-initio Simulation Package (version 5.4).[82] The core−valence interaction is described by the projector augmented wave (PAW) method.[83] The kinetic energy cutoff for the plane-wave expansion is set at 550 eV. The Monkhorst−Pack sampling with $6\times1\times1$ k-point grids is used. The ions and lattices are fully relaxed until the total energy and absolute value of the forces acting on each atom are less than 1×10^{-6} eV and 0.01 eV Å^{-1}, respectively. The distance between the polymer and its image (along y- and z-directions) as well as the polysulfide and its image (along all three directions), is set at least 12 Å in order to minimize the spurious interactions between the neighbouring images. The DFT-D3 method[84] was used to correct the dispersion interaction. The binding energy (E_b) is calculated using the equation: $E_b = (E_{polymer} + E_{Na_2S_x}) - E_{polymer + Na_2S_x}$ where $E_{polymer}$, $E_{Na_2S_x}$ and $E_{polymer + Na_2S_x}$ are the total energies of the pristine polymer, the polysulfide Na_2S_x (x=1-4) and the Na_2S_x binded polymer, respectively. The more positive the binding energy, the stronger the binding strength.

Journal of Materials Chemistry A

Conflicts of interest

The authors declare that they have no competing interests.

Acknowledgements

Footnotes

Electronic supplementary information (ESI) available.

References

1. E. Pomerantseva, F. Bonaccorso, X. Feng, Y. Cui and Y. Gogotsi, *Science*, 2019, **366**, eaan8285.

2. C. Ye, D. Chao, J. Shan, H. Li, K. Davey and S.-Z. Qiao, *Matter,* 2020, **2**, 323-344.

3. Y.-X. Wang, B. Zhang, W. Lai, Y. Xu, S.-L. Chou, H.-K. Liu and S.-X. Dou, *Adv. Energy Mater.,* 2017, **7**, 1602829.

4. Z. W. Seh, Y. Sun, Q. Zhang and Y. Cui, *Chem. Soc. Rev.,* 2016, **45**, 5605-5634.

5. S. Evers and L. F. Nazar, *Acc. Chem. Res.,* 2013, **46**, 1135–1143.

6. A. Manthiram, Y. Fu, S.-H. Chung, C. Zu and Y.-S. Su, *Chem. Rev.,* 2014, **114**, 11751–11787.

7. Y.-X. Wang, W.-H. Lai, S.-L. Chou, H.-K. Liu and S.-X. Dou, *Adv. Mater.,* 2020, **32**, 1903952.

8. C. Ye, Y. Jiao, D. Chao, T. Ling, J. Shan, B. Zhang, Q. Gu, K. Davey, H. Wang and S.-Z. Qiao, *Adv. Mater.,* 2020, **32**, 1907557.

9. W. Luo, F. Shen, C. Bommier, H. Zhu, X. Ji and L. Hu, *Acc. Chem. Res.,* 2016, **49**, 231-240.

Journal of Materials Chemistry A Accepted Manuscript

10. V. Kumar, A. Y. S. Eng, Y. Wang, D.-T. Nguyen, M.-F. Ng and Z. W. Seh, *Energy Storage Mater.,* 2020, **29**, 1–8.

11. X. Zheng, H. Fu, C. Hu, H. Xu, Y. Huang, J. Wen, H. Sun, W. Luo and Y. Huang, *J. Phys. Chem. Lett.,* 2019, **10**, 707-714.

12. N. Wang, Y. Wang, Z. Bai, Z. Fang, X. Zhang, Z. Xu, Y. Ding, X. Xu, Y. Du, S. Dou and G. Yu, *Energy Environ. Sci.,* 2020, **13**, 562-570.

13. X. Xu, D. Zhou, X. Qin, K. Lin, F. Kang, B. Li, D. Shanmukaraj, T. Rojo, M. Armand and G. Wang, *Nat. Commun.,* 2018, **9**, 3870.

14. Y. Lee, J. Lee, J. Lee, K. Kim, A. Cha, S. Kang, T. Wi, S. Kang, H. Lee and N. Choi, *ACS Appl. Mater. Interfaces,* 2018, **10**, 15270-15280.

15. V. Kumar, Y. Wang, A. Y. S. Eng, M.-F. Ng and Z. W. Seh, *Cell Rep. Phys. Sci.*, 2020, **1**, 100044.

16. I. Bauer, M. Kohl, H. Althues and S. Kaskel, *Chem. Commun.,* 2014, **50**, 3208.

17. Y. Li, W. Wang, X. Liu, E. Mao, M. Wang, G. Li, L. Fu, Z. Li, A. Y. S. Eng, Z. W. Seh and Y. Sun, *Energy Storage Mater.,* 2019, **23**, 261-268.

18. X. Yu and A. Manthiram, *J. Phys. Chem. Lett.,* 2014, **5**, 1943−1947.

19. C.-W. Park, J.-H. Ahn, H.-S. Ryu, K.-W. Kim and H.-J. Ahn, *Electrochem. Solid-State Lett.,* 2006, **9**, A123-A125.

20. L. Xu, J. Li, W. Deng, H. Shuai, S. Li, Z. Xu, J. Li, H. Hou, H. Peng, G. Zou and X. Ji, *Adv. Energy Mater.* 2020, DOI: 10.1002/aenm.202000648.

21. X. Yu and A. Manthiram, *Matter,* 2019, **1**, 1–13.

22. X. Hu, Y. Ni, C. Wang, H. Wang, E. Matios, J. Chen and W. Li, *Cell Rep. Phys. Sci.,* 2020, **1**, 100015.

23. Z. Jiang, S. Wang, X. Chen, W. Yang, X. Yao, X. Hu, Q. Han and H. Wang, *Adv. Mater.*, 2020, **32**, 1906221.

24. Z. Jiang, H. Xie, S. Wang, X. Song, X. Yao and H. Wang, *Adv. Energy Mater.*, 2018, **8**, 1801433.

25. X. Chen, W. He, L.-X. Ding, S. Wang and H. Wang, *Energy Environ. Sci.*, 2019, **12**, 938-944.

26. C. Wang, H. Wang, X. Hu, E. Matios, J. Luo, Y. Zhang, X. Lu and W. Li, *Adv. Energy Mater.,* 2018, **9**, 1803251.

27. Z. Yan, J. Xiao, W. Lai, L. Wang, F. Gebert, Y. Wang, Q. Gu, H. Liu, S.-L. Chou, H. Liu and S. X. Dou, *Nat. Commun.*, 2019, **10**, 4793.

28. A. Y. S. Eng, J. L. Cheong and S. S. Lee, *Appl. Mater. Today*, 2019, **16**, 529-537.

29. Y. Li, C. Wang, W. Wang, A. Y. S. Eng, M. Wan, L. Fu, E. Mao, G. Li, J. Tang, Z. W. Seh and Y. Sun, *ACS Nano,* 2019, **14**, 1148-1157.

30. Z. Sun, S. Vijay, H. H. Heenen, A. Y. S. Eng, W. Tu, Y. Zhao, S. Koh, P. Gao, Z. W. Seh, K. Chan and H. Li, *Adv. Energy Mater.,* 2020, **10**, 1904010.

31. C. Ye, L. Zhang, C. Guo, D. Li, A. Vasileff, H. Wang and S.-Z. Qiao, *Adv. Funct. Mater.*, 2017, **27**, 1702524.

32. C. Ye, Y. Jiao, H. Jin, A. D. Slattery, K. Davey, H. Wang and S.-Z. Qiao, *Angew. Chem. Int. Ed.*, 2018, **57**, 16703−16707.

33. J. W. Jeon, D.-M. Kim, J. Lee, J.-C. Lee, Y. S. Kim, K. T. Lee and B. G. Kim, *J. Mater. Chem. A,* 2020, **8**, 3580-3585.

34. S. Wei, S. Xu, A. Agrawral, S. Choudhury, Y. Lu, Z. Tu, L. Ma and L. Archer, *Nat. Commun.,* 2016, **7**, 11722.

35. Y.-M. Chen, W. Liang, S. Li, F. Zou, S. M. Bhaway, Z. Qiang, M. Gao, B. D. Vogt and Y. Zhu, *J. Mater. Chem. A,* 2016, **4**, 12471.

36. I. Kim, C. Kim, S. Choi, J. Ahn, J. Ahn, K. Kim, E. Cairns and H. Ahn, *J. Power Sources,* 2016, **307**, 31-37.

37. T. Hwang, D. Jung, J. Kim, B. Kim and J. Choi, *Nano Lett.,* 2013, **13**, 4532-4538.

38. J. Wang, J. Yang, Y. Nuli and R. Holze, *Electrochem. Commun.,* 2007, **9**, 31−34.

39. T. Wu, M. Jing, L. Yang, G. Zou, H. Hou, Y. Zhang, Y. Zhang, X. Cao and X. Ji, *Adv. Energy Mater.,* 2019, **9**, 1803478.

40. T. Wu, M. Jing, Y. Tian, L. Yang, J. Hu, X. Cao, G. Zou, H. Hou and X. Ji, *Adv. Funct. Mater.,* 2019, **29**, 1900941.

41. S. Ma, P. Zuo, H. Zhang, Z. Yu, C. Cui, M. He and G. Yin, *Chem. Commun.,* 2019, **55**, 5267.

42. T. An, H. Jia, L. Peng and J. Xie, *ACS Appl. Mater. Interfaces,* 2020, **12**, 20563−20569.

43. Z. Li, J. Zhang, Y. Lu and X. W. Lou, *Sci. Adv.,* 2018, **4**, eaat1687.

44. S. Li, Z. Zeng, J. Yang, Z. Han, W. Hu, L. Wang, J. Ma, B. Shan and J. Xie, *ACS Appl. Energy Mater.,* 2019, **2**, 2956-2964.

45. Z. W. Seh, Q. Zhang, W. Li, G. Zheng, H. Yao and Y. Cui, *Chem. Sci.,* 2013, **4**, 3673.

46. L. Li, T. Pascal, J. Connell, F. Fan, S. Meckler, L. Ma, Y. Chiang, D. Prendergast and B. Helms, *Nat. Commun.,* 2017, **8**, 2277.

47. J. Liao, Z. Liu, J. Wang and Z. Ye, *ACS Omega,* 2020, **5**, 8272-8282.

Journal of Materials Chemistry A Accepted Manuscript

48. H. M. Kim, J.-Y. Hwang, D. Aurbach and Y.-K. Sun, *J. Phys. Chem. Lett.,* 2017, **8**, 5331-5337.

49. E. Peled, M. Goor, I. Schektman, T. Mukra, Y. Shoval and D. Golodnitsky. *J. Electrochem. Soc.,* 2017, **164**, A5001-A5007.

50. Y. Li, Q. Zeng, I. R. Gentle and D.-W. Wang, *J. Mater. Chem. A,* 2017, **5**, 5460-5465.

51. I. Kovalenko, B. Zdyrko, A. Magasinski, B. Hertzberg, Z. Milicev, R. Burtovyy, I. Luzinov and G. Yushin, *Science,* 2011, **334**, 75-79.

52. Q. Guo and Z. Zheng, *Adv. Funct. Mater.,* 2020, **30**, 1907931.

53. W. Chen, T. Lei, T. Qian, W. Lv, W. He, C. Wu, X. Liu, J. Liu, B. Chen, C. Yan and J. Xiong. *Adv. Energy Mater.*, 2018, **8**, 1702889.

54. R. J. Ouellette and J. D. Rawn, in *Organic Chemistry: Structure, Mechanism, Synthesis*, Elsevier Inc., London, UK, 2nd Ed., 2018.

55. S. Jiang, L. Jin, H. Hou and L. Zhang, in *Polymer-Based Multifunctional Nanocomposites and Their Applications*, eds. K. Song, C. Liu and J. Z. Guo, Elsevier, Amsterdam, 2019, Chapter 8 - Polymer-Based Nanocomposites with High Dielectric Permittivity, pages 201-243.

56. L. Ruan, X. Yao, Y. Chang, L. Zhou, G. Qin and X. Zhang, *Polymers,* 2018, **10**, 228.

57. C. Y. Liang and S. Krimm, *J. Polym. Sci.,* 1958, **31**, 513–522.

58. R. F. Ribeiro, L. C. Pardini , N. P. Alves, and C. A. R. Brito Jr., *Polímeros,* 2015, **25**, 523-530.

59. J. Fanous, M. Wegner, J. Grimminger, Ä. Andresen and M. R. Buchmeiser, *Chem. Mater.,* 2011, **23**, 5024-5028.

60. S. Wei, L. Ma, K. E. Hendrickson, Z. Tu and L. A. Archer, *J. Am. Chem. Soc.,* 2015, **137**, 12143-12152.

61. Z. Q. Jin, Y. Liu, W. Wang, A. Wang, B. Hu, M. Shen, T. Gao, P. Zhao and Y. Yang, *Energy Storage Mater.,* 2018, **14**, 272-278.

62. W. Wang, Z. Cao, G. Elia, Y. Wu, W. Wahyudi, E. Abou-Hamad, A. Emwas, L. Cavallo, L. Li and J. Ming, *ACS Energy Lett.,* 2018, **3**, 2899-2907.

63. T. Zhu, X. Dong, Y. Liu, Y. Wang, C. Wang and Y. Xia, *ACS Appl. Energy Mater.,* 2019, **2**, 5263-5271.

64. J. Fanous, M. Wegner, J. Grimminger, M. Rolff, M. B. M. Spera, M. Tenzer and M. R. Buchmeiser, *J. Mater. Chem.,* 2012, **22**, 23240-23245.

65. A. Nogaj, C. Süling and M. Schweizer, in *Ullmann's Polymers and Plastics: Products and Processes,* ed. B. Elvers, Wiley-VCH, Weinheim, Germany, 7th Edition, 2016, Volume 4, Part 3, Polyacrylonitrile Fibers, pages 1513-1528.

Journal of Materials Chemistry A Accepted Manuscript

Journal of Materials Chemistry A

66. J. Yue, F. Han, X. Fan, X. Zhu, Z. Ma, J. Yang and C. Wang. *ACS Nano,* 2017, **11**, 4885−4891.

67. K. Mereiter, A. Preisinger, A. Zellner, W. Mikenda and H. Steidl, *J. Chem. Soc. Dalton Trans.,* 1984, 1275-1277.

68. K. M. Abraham and S. M. Chaudhri, *J. Electrochem. Soc.,* 1986, **133**, 1307.

69. M. Fantauzzi, B. Elsener, D. Atzei, A. Rigoldi and A. Rossi, *RSC Adv.,* 2015, **5**, 75953–75963.

70. A. Y. S. Eng, C. K. Chua and M. Pumera, *Electrochem. Commun,.* 2015, **59**, 86-90.

71. Z. Lin, Q. Xia, W. Wang, W. Li and S. Chou, *InfoMat.,* 2019, **1**, 376–389.

72. C. Zhao, Y. Lu, L. Chen and Y.-S. Hu, *InfoMat.*, 2020, **2**, 126–138.

73. K. C. Kim, T. Liu, K. H. Jung, S. W. Lee and S. S. Jang, *Energy Storage Mater.,* 2019, **19**, 242–250.

74. A. Magasinski, B. Zdyrko, I. Kovalenko, B. Hertzberg, R. Burtovyy, C. Huebner, T. Fuller, I. Luzinov and G. Yushin, *ACS Appl. Mater. Interfaces,* 2010, **2**, 3004-3010.

75. M. C. Militello and S. W. Gaarenstroom, *Surf. Sci. Spectra,* 1999, **6**, 141.

76. L. Hencz, H. Chen, H. Y. Ling, Y. Wang, C. Lai, H. Zhao and S. Zhang, *Nano-Micro Lett.,* 2019, **11**, 17.

77. W.-R. Liu, M.-H. Yang, H.-C. Wu, S. M. Chiao and N.-L. Wu, *Electrochem. Solid-State Lett.,* 2005, **8**, A100-A103.

78. M. Shaibani, M. Mirshekarloo, R. Singh, C. Easton, M. Cooray, N. Eshraghi, T. Abendroth, S. Dörfler, H. Althues, S. Kaskel, A. Hollenkamp, M. Hill and M. Majumder, *Sci. Adv.,* 2020, **6**, eaay2757.

79. Materials Studio software suite, BIOVIA, San Diego, CA, 2017.

80. BIOVIA Dreiding, Forcite, Materials Studio software, BIOVIA, San Diego, CA, 2017.

81. J. P. Perdew, K. Burke and M. Ernzerhof, *Phys. Rev. Lett.,* 1996, **77**, 3856-3868.

82. G. Kresse and J. Furthmuller, *Phys. Rev. B*, 1996, **54**, 11169-11186.

83. P. E. Blöchl, *Phys. Rev. B,* 1994, **50**, 17953-17979.

84. S. Grimme, J. Antony, S. Ehrlich and H. Krieg, *J. Chem. Phys*., 2010, **132**, 154104.

Journal of Materials Chemistry A Accepted Manuscript

Tailoring Binder-Cathode Interactions for Long-Life Room-Temperature Sodium-Sulfur Batteries

Alex Yong Sheng Eng,[a] Dan-Thien Nguyen,[a] Vipin Kumar,[a] Gomathy Sandhya Subramanian,[a] Man-Fai Ng,[b] and Zhi Wei Seh[a]*

Table of Contents

Strong interactions between carboxyl binder groups and short-chain sodium polysulfides prevent capacity loss and maintain structural integrity of sulfur cathodes.

Journal of Materials Chemistry A Accepted Manuscript